LETTER

XFEL structures of the human MT₂ melatonin receptor reveal the basis of subtype selectivity

Linda C. Johansson^{1,2,14}, Benjamin Stauch^{1,2,14}, John D. McCorvy^{3,13}, Gye Won Han^{1,2}, Nilkanth Patel^{1,4}, Xi-Ping Huang^{3,5}, Alexander Batyuk⁶, Cornelius Gati^{7,8}, Samuel T. Slocum^{3,5}, Chufeng Li^{9,10}, Jessica M. Grandner^{1,4}, Shuming Hao^{1,2}, Reid H. J. Olsen³, Alexandra R. Tribo³, Sahba Zaare⁹, Lan Zhu¹⁰, Nadia A. Zatsepin^{9,10}, Uwe Weierstall^{9,10}, Saïd Yous¹¹, Raymond C. Stevens^{1,2,4}, Wei Liu¹⁰, Bryan L. Roth^{3,5,12*}, Vsevolod Katritch^{1,2,4*} & Vadim Cherezov^{1,2,4*}

The human MT₁ and MT₂ melatonin receptors^{1,2} are G-proteincoupled receptors (GPCRs) that help to regulate circadian rhythm and sleep patterns³. Drug development efforts have targeted both receptors for the treatment of insomnia, circadian rhythm and mood disorders, and cancer³, and MT₂ has also been implicated in type 2 diabetes^{4,5}. Here we report X-ray free electron laser (XFEL) structures of the human MT₂ receptor in complex with the agonists 2-phenylmelatonin (2-PMT) and ramelteon⁶ at resolutions of 2.8 Å and 3.3 Å, respectively, along with two structures of function-related mutants: H208^{5,46}A (superscripts represent the Ballesteros-Weinstein residue numbering nomenclature⁷) and N86^{2.50}D, obtained in complex with 2-PMT. Comparison of the structures of MT₂ with a published structure⁸ of MT₁ reveals that, despite conservation of the orthosteric ligand-binding site residues, there are notable conformational variations as well as differences in [3H] melatonin dissociation kinetics that provide insights into the selectivity between melatonin receptor subtypes. A membraneburied lateral ligand entry channel is observed in both MT₁ and MT₂, but in addition the MT₂ structures reveal a narrow opening towards the solvent in the extracellular part of the receptor. We provide functional and kinetic data that support a prominent role for intramembrane ligand entry in both receptors, and suggest that there might also be an extracellular entry path in MT₂. Our findings contribute to a molecular understanding of melatonin receptor subtype selectivity and ligand access modes, which are essential for the design of highly selective melatonin tool compounds and therapeutic agents.

To improve the low surface expression and stability of wild-type MT₂, we introduced eight point mutations on the basis of homology to other class A receptors: D86^{2.50}N (ref. ⁹), L108^{ECL1}F, F129^{3.41}W (ref. ¹⁰), N137^{3.49}D, C140^{3.52}L, W264^{6.48}F, A305^{7.50}P, and N312^{8.47}D; these were essential for determination of the high-resolution structure of both MT₂ and MT₁⁸. To promote crystal contacts, we used a double-fusion approach, with rubredoxin¹¹ in the intracellular loop 3 (ICL3) and thermostabilized apocytochrome b_{562} RIL (BRIL)¹¹ attached to the receptor N terminus. Radioligand binding assays revealed a 120-fold reduction in melatonin binding affinity (approximately 30-fold reduction at physiological concentration of NaCl), probably owing to stabilization of the crystallized construct in an inactive 'low agonist affinity' state that is deficient in G-protein coupling and signalling^{9,12} (Extended Data Table 1). All four MT₂ structures were obtained using lipidic cubic phase (LCP)¹³ crystallization (Extended Data Fig. 1, Extended Data Table 2). The overall receptor conformation was similar in all four

structures ($C\alpha$ root mean squared deviation (r.m.s.d.) < 0.3 Å), so we used the highest resolution MT₂–2-PMT structure in the analysis below unless otherwise noted.

 MT_2 adopts the canonical seven-transmembrane-domain (7TM) fold of class A receptors, with the short amphipathic helix VIII parallel to the membrane on the intracellular side (Fig. 1a). As in MT_1^8 , the 7TM bundle of MT_2 is found in an inactive conformation. Restoration of the function-impairing D86²-50N mutation (Extended Data Table 3) allowed us to solve the $MT_2(N86D)$ –2-PMT structure at a lower resolution and showed that this mutation had no major effect on the overall

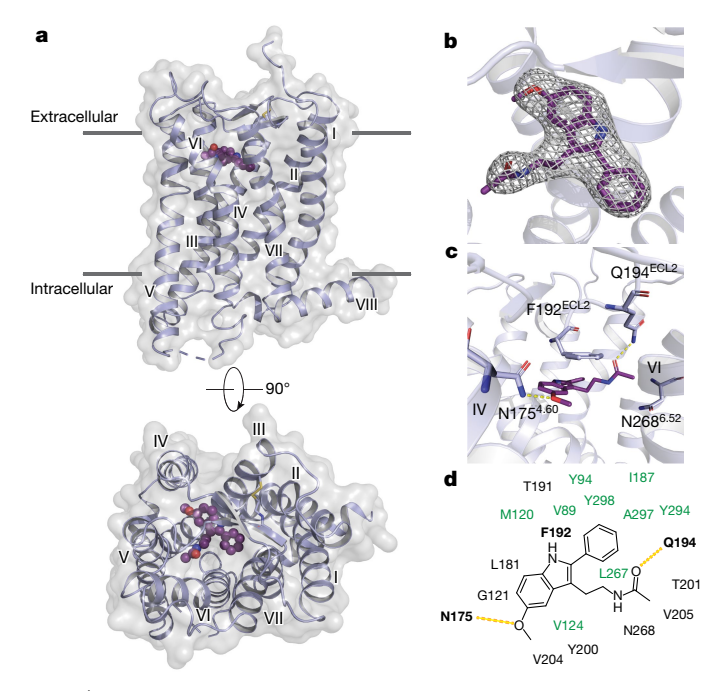


Fig. 1 | Overview of the MT₂ structure. a, Overview of MT₂ (violet) shows the canonical 7TM topology, with the ligand 2-PMT (purple) in the binding pocket. A 90° view shows the receptor from the extracellular side. Approximate membrane boundaries are shown as grey lines. b, $2mF_0 - DF_c$ density (grey mesh) of 2-PMT contoured at 1σ . c, Binding pocket with key ligand interaction residues. d, Schematic diagram of ligand-interacting residues. Residues in the hydrophobic subpocket are coloured green. Hydrogen bonds are shown as dashed yellow lines in c, d.

¹Bridge Institute, USC Michelson Center for Convergent Biosciences, University of Southern California, Los Angeles, CA, USA. ²Department of Chemistry, University of Southern California, Los Angeles, CA, USA. ³Department of Pharmacology, University of North Carolina at Chapel Hill, NC, USA. ⁴Department of Biological Sciences, University of Southern California, Los Angeles, CA, USA. ⁵National Institute of Mental Health Psychoactive Drug Screening Program, University of North Carolina at Chapel Hill, Chapel Hill, NC, USA. ⁶Linac Coherent Light Source, SLAC National Accelerator Laboratory, Menlo Park, CA, USA. ⁷Bioscience Division, SLAC National Accelerator Laboratory, Menlo Park, CA, USA. ⁸Department of Structural Biology, Stanford University, Stanford, CA, USA. ⁹Department of Physics, Arizona State University, Tempe, AZ, USA. ¹⁰School of Molecular Sciences and Biodesign Center for Applied Structural Discovery, Biodesign Institute, Arizona State University, Tempe, AZ, USA. ¹¹Université de Lille, CHU Lille, Inserm, UMR-S 1172 - JPArc - Centre de Recherche Jean-Pierre AUBERT Neurosciences et Cancer, Lille, France. ¹²Division of Chemical Biology and Medicinal Chemistry, Eshelman School of Pharmacy, University of North Carolina at Chapel Hill, Chapel Hill, NC, USA. ¹³Present address: Department of Cell Biology, Neurobiology and Anatomy, Medical College of Wisconsin, Milwaukee, WI, USA. ¹⁴These authors contributed equally: Linda C. Johansson, Benjamin Stauch. *e-mail: bryan_roth@med.unc.edu; katritch@usc.edu; cherezov@usc.edu

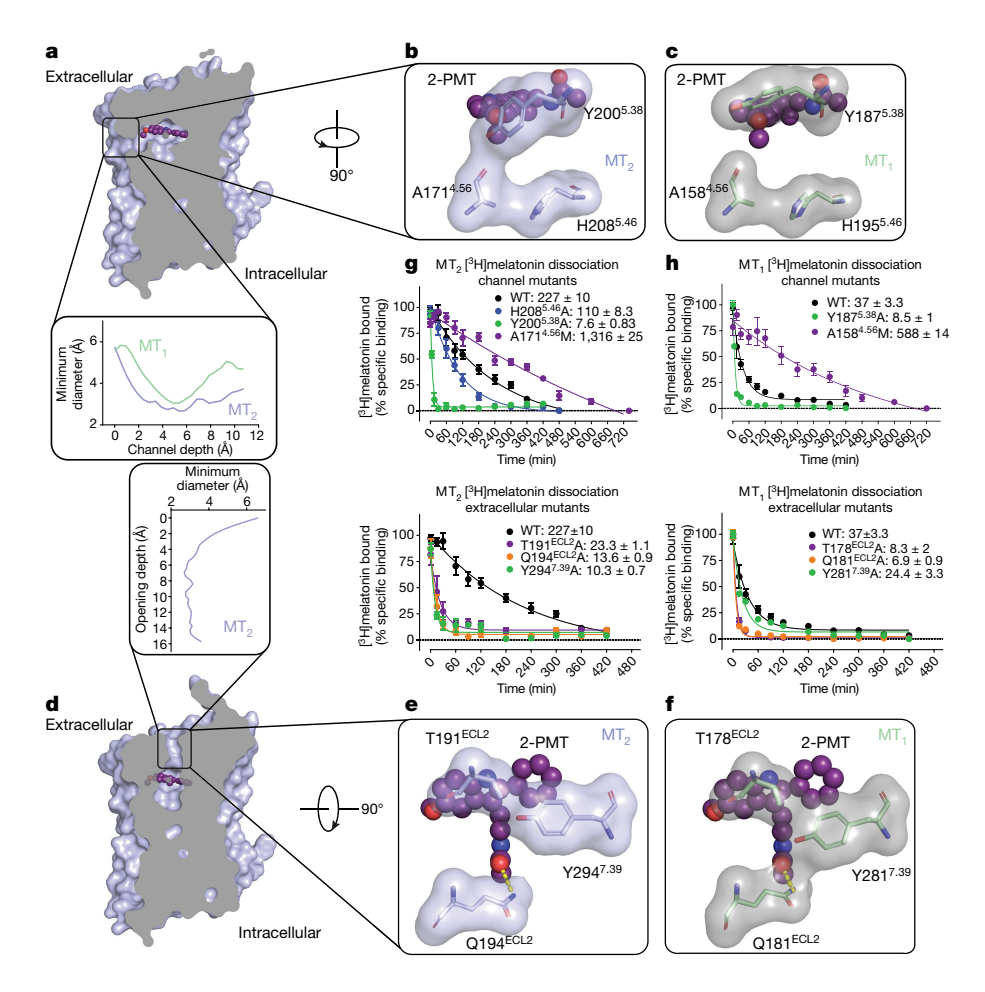


Fig. 2 | Two possible ligand entries in MT_2 . a, View of the membrane-buried channel in MT_2 . Inset, channel diameter profile across its length for MT_1 and MT_2 . b, A 90° view of the channel in MT_2 , highlighting three residues discussed in the text. c, The same view as in b of MT_1 (green) showing a different conformation of Y187^{5,38} that widens the channel compared to MT_2 . d, View of the ECL opening found in MT_2 (violet) with 2-PMT (purple). Inset, ECL opening profile across the length.

receptor conformation, as also supported by molecular dynamics simulations (Supplementary Fig. 1). Structural comparison of MT2 and MT₁—which share 68% sequence identity—revealed notable overall similarity ($C\alpha$ r.m.s.d. < 0.6 Å), with all ligand-interacting residues conserved8 (Fig. 1d, Extended Data Fig. 2c). There is a common pharmacophore between receptor subtypes that consists of aromatic stacking of the ligand core with F192^{ECL2}, as well as hydrogen bonds between the methoxy group of 2-PMT and N175^{4.60} and between the alkylamide tail of the ligand and Q194^{ECL2} (Fig. 1c, d). The stability of these ligand-anchoring interactions was confirmed by molecular dynamics simulations (Extended Data Fig. 3). Further, mutation of F192^{ECL2} to isoleucine or alanine caused loss of ligand binding and signalling (Extended Data Tables 1, 4), as also observed for MT₁⁸. In contrast to MT₁, however, mutation of N175^{4.60} to alanine in MT₂ did not impair receptor function, which indicates that this residue has different roles in the activation of the two receptor subtypes. Mutation of either Q194 $^{\rm ECL2}$ or N268^{6.52} to alanine had only minor effects on receptor ligand affinity, receptor activation or stability (Extended Data Tables 1, 4, 5), whereas the double mutation Q194 ECL2 A/N268 $^{6.52}$ A results in a marked loss of receptor activity (Extended Data Tables 4, 5), which suggests that these residues show functional redundancy in MT2. Notably, despite the binding site residues being conserved between the two receptors, we observed subtle conformational differences between them, such as in the side chains of Y200^{5,38} and Y294^{7,39} and in the backbone region surrounding P174^{4.59} (Extended Data Fig. 2d). Furthermore, the binding

e, A 90° view through the ECL opening in MT₂, highlighting three residues discussed in the text. **f**, The same view as in **e** of MT₁ (green), showing a different conformation of Y281^{7,39} that seals the ECL opening. **g**, [³H] Melatonin dissociation kinetics for MT₂ membrane channel mutants (top) and ECL opening mutants (bottom). **h**, As in **g** for MT₁. Residence time (k_{off}^{-1}) in **g** and **h** is given in minutes. Data are shown as mean \pm s.e.m. for n=3 independent experiments.

pocket of MT_2 is about 50 Å³ (7%) larger than that of MT_1 , with most of the volume difference attributed to the region around the alkylamide tail and the hydrophobic subpocket that accommodates substituents of melatonin analogues in our structures (Fig. 1d, Extended Data Fig. 2b). These regions have a key role in MT_2 selectivity, as discussed below.

Structural analysis of MT2 revealed an opening between helices IV and V from the orthosteric ligand binding site to the membrane (Fig. 2a). This channel is similar to that seen in MT₁, but is more constricted (around 2.6 Å in diameter at the narrowest part). Comparison of the structures of MT_2 and MT_1 revealed that $Y200^{5.38}$ in MT_2 makes a hydrogen bond to N175 $^{4.60}$, constricting the channel, whereas in MT₁ it adopts a different conformation, pointing towards the lipid interface (Fig. 2a-c, Extended Data Fig. 2c, d). In our MT₂(H208A)-2-PMT structure, mutating H208^{5.46} near the channel entrance to alanine further closes off the opening by an approximately 0.9 Å inward shift of helix V (Extended Data Fig. 4). This finding suggests that H208^{5,46} helps to control the channel entrance, albeit only moderately influencing ligand affinity and receptor function in MT2 (Extended Data Tables 1, 4). Further analysis of the MT₂ structures revealed a potential secondary access route to the orthosteric binding site from the solvent-exposed extracellular (ECL) region (Fig. 2d). This second opening has a slightly larger diameter (about 2.5–3 Å) and is lined by aromatic Y294^{7.39} and hydrophilic T191^{ECL2} and Q194^{ECL2} residues (Fig. 2e). In MT₁, the corresponding residues Q181^{ECL2} and Y281^{7.39} adopt different conformations, completely sealing off this entrance (Fig. 2f).

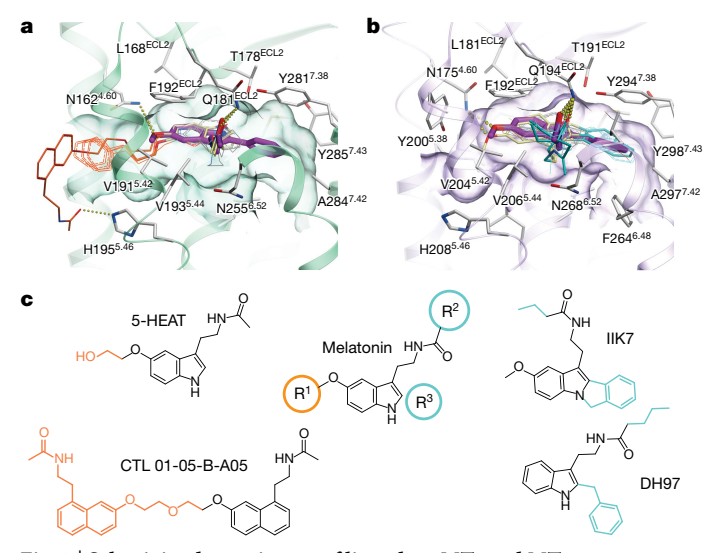


Fig. 3 | Selectivity determinants of ligands at MT1 and MT2. a, Docking of selective ligands into MT1 (green), with 2-PMT (purple) from the crystal structure shown as reference. Ligands selective for MT1 (compounds 63, 64, 65a, and 65b) 17 are shown in grey. Two representative ligands, 5-HEAT16 and CTL 01-05-B-A058 are coloured pale yellow, with their selectivity-conferring substituents (R1 position) shown in orange. b, Docking of ligands into MT2 (violet), with 2-PMT (purple) shown as reference. Non-selective (tasimelteon, TIK301 17) and selective (UCM1014 20 , K185 17 , and 4P-PDOT 17) ligands are shown in grey. Two representative ligands, DH97 18 and IIK7 17 are coloured pale yellow, with selectivity-conferring substituents (R2 and R3 positions) shown in cyan. Predicted hydrogen bonds are shown as dotted lines in a, b. c, Melatonin SAR, in which R1 substituents confer MT1 selectivity (orange), and substituents in R2 and R3 positions confer MT2 selectivity (cyan). See Supplementary Table 1 for a list of all docked ligands.

To test the relative importance of these two putative binding site access routes, we performed kinetic ligand dissociation studies on both receptors using [$^3\mathrm{H}$]melatonin as a tracer. The ligand residence time (k_{off}^{-1}) is substantially longer in wild-type MT $_2$ than in MT $_1$, which suggests that the narrower membrane entry channel restricts ligand access (Fig. 2g, h). Mutation of the membrane channel-lining residue Y $^{5.38}\mathrm{A}$, designed to widen the access channel, caused a 30-fold decrease in residence time for MT $_2$ (with similar ligand affinity), while the corresponding mutation in MT $_1$ caused a more-modest decrease in residence time, consistent with the wider channel and a different conformation of Y $^{5.38}$ in MT $_1$. To constrict the channel, we mutated A $^{4.56}$, a key residue at the interface of helices IV and V in both receptors, into a bulkier methionine. This mutation markedly increased residence time for both receptors (Fig. 2g, h), reaching up to 20 h in MT $_2$, which suggests that this channel is important for ligand access in both receptors.

When we tested mutations designed to widen the ECL opening in both receptors, ligand residence time was reduced more than tenfold in MT $_2$ mutants T191 $^{\rm ECL2}$ A and Q194 $^{\rm ECL2}$ A, and roughly fivefold with the equivalent ECL2 mutations in MT $_1$ (Fig. 2g, h). The MT $_2$ (Y294 $^{7.39}$ A) mutant showed an even greater decrease in ligand residence time (22-fold) relative to the wild type, whereas the equivalent MT $_1$ mutant showed a similar residence time to the wild type. These differences can be reconciled if ligand site access through the ECL entrance is more important in MT $_2$ than in MT $_1$, consistent with the crystal structures, in which residue Y294 $^{7.39}$ adopts a different conformation in MT $_2$, allowing easier ligand egress through the ECL opening.

The elucidation of high-resolution structures of both melatonin receptor subtypes and published ligand structure–activity relationship (SAR) data 14,15 allowed us to establish a model of receptor subtype ligand selectivity. To this end, we used molecular docking of several available selective ligands to both receptors. Docking of the moderately MT_1 -selective compound 5-hydroxyethoxy-N-acetyltryptamine

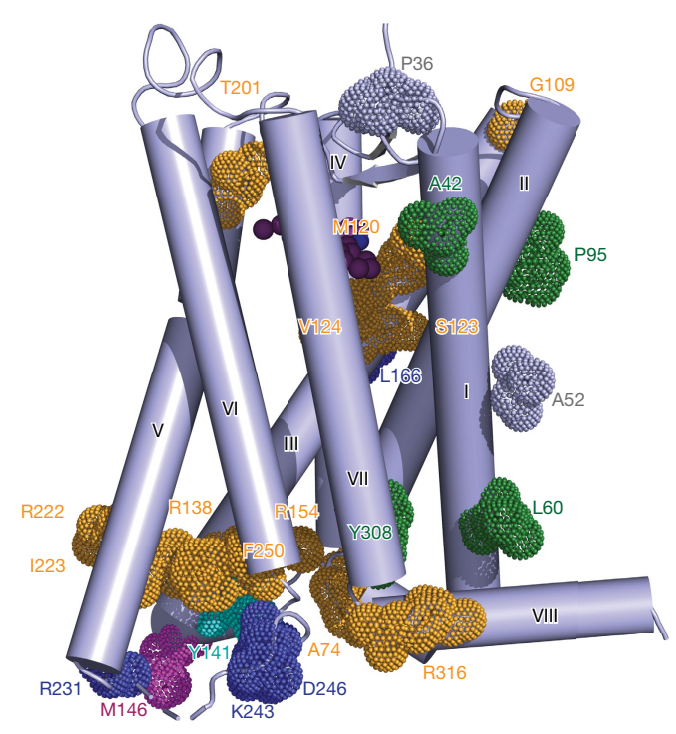


Fig. 4 | MT₂ mutations implicated in type 2 diabetes. Mapping of residues implicated in type 2 diabetes^{4,5} onto the MT₂ crystal structure. Gold, residues in which mutations lead to defects in two or more pathways; cyan, G-protein-specific defects; blue, β -arrestin-2-specific defects; magenta, ERK-specific defects; green, mutations that abolish melatonin binding; grey, mutations similar to the wild type. Type-2-diabetes-related mutations in residues not observed in the crystal structure are not shown.

(5-HEAT)¹⁶ and the bitopic ligand CTL 01-05-B-A05⁸ suggests that—although an extension or substitution of the R¹ position by a linear alkyl chain can be accommodated by the membrane access channel in both MT₁ and MT₂ (Fig. 3a, c)—the narrower MT₂ channel renders binding of the extended portion of the bitopic ligands suboptimal owing to potential steric clashes. Accordingly, the H208^{5,46}A mutation in MT₂ abolished the efficacy of CTL 01-05-B-A05 as a G_i agonist (Extended Data Fig. 4d), probably by further restriction the channel and/or eliminating the hydrogen bond between H208^{5,46} and CTL 01-05-B-A05 that was observed in docking to MT₁⁸. This mutation had a negligible effect on monotopic ligand binding and function (Extended Data Tables 1, 4, 5), which suggests that a sufficiently wide membrane channel (as in MT₁) is essential for accommodation of bitopic ligands.

The MT₂-selective ligands IIK7 and DH97 (both of which are about 90-fold selective)^{17,18} adopt 'tail up' binding modes similar to that of 2-PMT, with their alkylamide tails (R² position in Fig. 3b, c) interacting with Q194^{ECL2}. By contrast, in MT₁ the longer alkylamide tails of these ligands avoid this upward tail position owing to steric clashes, and can adopt only suboptimal 'tail down' conformations. Bulky substituents in the R³ position confer MT₂ selectivity by using the larger hydrophobic subpocket of the receptor (Fig. 3b, c). In summary, our analysis suggests that R¹ substituents are important for MT₁ selectivity, while R² and R³ mostly convey selectivity towards MT₂ (Fig. 3c). The slightly larger binding site in MT₂ also helps to achieve selectivity, as reflected by the larger number of compounds that are moderately selective for MT₂ (Extended Data Fig. 5).

Subtype-selective compounds are desirable owing to the involvement of MT_2 in type 2 diabetes, for which a number of single nucleotide polymorphisms (SNPs) have been reported^{4,5}. When we mapped these sites onto our MT_2 structure, we observed clustering of residues in the vicinity of the ligand binding pocket and on the receptor surface, along the membrane interface of helices I and II and the intracellular G-protein and β -arrestin binding regions (Fig. 4). The exposed positions

RESEARCH LETTER

of these residues could point to their involvement in interactions with intracellular and membrane partners. Other instances of SNPs associated with type 2 diabetes include P95 $^{2.59}\mathrm{L}$ of the YPYP motif, which is involved in receptor stability and function in MT $_1^8$, and mutations in known microswitches such as R138 $^{3.50}\mathrm{H/L/C}$ of the E/DRY motif 19 and Y308 $^{7.53}\mathrm{S}$ of the NPXXY motif 12 . Although none of the analysed SNPs is involved in direct interactions with melatonin, the M120 $^{3.32}\mathrm{I/V}$ and V124 $^{3.36}\mathrm{I}$ variants are located in the hydrophobic subpocket of the receptor, which could influence ligand binding and affect subsequent signalling pathways $^{4.5}$.

The structural basis of melatonin receptor subtype selectivity revealed here has the potential to inspire a new generation of highly selective pharmacological tools that will help to further dissect the melatonin system. We also provide insights into differences in ligand entry between the two receptors by demonstrating the potential of MT₂ to support extracellular ligand access to the binding pocket. This difference in ligand entry can be exploited to facilitate melatonin receptor subtype selectivity, as the ECL route in MT₂ could accommodate more polar compounds compared to the membrane-buried channel. We therefore expect that our results will lead to new therapies involving these pleiotropic receptors, aimed at—but not limited to—the treatment of type 2 diabetes, cancer and sleep disorders.

Online content

Any methods, additional references, Nature Research reporting summaries, source data, statements of data availability and associated accession codes are available at https://doi.org/10.1038/s41586-019-1144-0.

Received: 28 July 2018; Accepted: 26 March 2019; Published online 24 April 2019.

- Reppert, S. M., Weaver, D.R. & Ebisawa, T. Cloning and characterization of a mammalian melatonin receptor that mediates reproductive and circadian responses. *Neuron* 13, 1177–1185 (1994).
- Reppert, S. M. et al. Molecular characterization of a second melatonin receptor expressed in human retina and brain: the Mel1b melatonin receptor. Proc. Natl Acad. Sci. USA 92, 8734–8738 (1995).
- Liu, J. et al. MT1 and MT2 melatonin receptors: a therapeutic perspective. Annu. Rev. Pharmacol. Toxicol. 56, 361–383 (2016).
- Bonnefond, A. et al. Rare MTNR1B variants impairing melatonin receptor 1B function contribute to type 2 diabetes. Nat. Genet. 44, 297–301 (2012).
- Karamitri, A. et al. Type 2 diabetes-associated variants of the MT2 melatonin receptor affect distinct modes of signaling. Sci. Signal. 11, eaan6622 (2018).
- Kato, K. et al. Neurochemical properties of ramelteon (TAK-375), a selective MT1/MT2 receptor agonist. Neuropharmacology 48, 301–310 (2005).
- Ballesteros, J. A. & Weinstein, H. Integrated methods for the construction of three-dimensional models and computational probing of structure-function relations in G protein-coupled receptors. *Meth. Neurosci.* 25, 366–428 (1995).
- Stauch, B. et al. Structural basis of ligand recognition at the human MT1 melatonin receptor. Nature https://doi.org/10.1038/s41586-019-1141-3 (2019).
- White, K. L. et al. Structural connection between activation microswitch and allosteric sodium site in GPCR signaling. Structure 26, 259–269.e5 (2018).
 Roth, C. B., Hanson, M. A. & Stevens, R. C. Stabilization of the human
- Roth, C. B., Hanson, M. A. & Stevens, R. C. Stabilization of the human β2-adrenergic receptor TM4–TM3–TM5 helix interface by mutagenesis of Glu122^{3,41}, a critical residue in GPCR structure. J. Mol. Biol. 376, 1305–1319 (2008)
- Chun, E. et al. Fusion partner toolchest for the stabilization and crystallization of G protein-coupled receptors. Structure 20, 967–976 (2012).
- Audet, M. & Bouvier, M. Restructuring G-protein-coupled receptor activation. Cell 151, 14–23 (2012).
- Caffrey, M. & Cherezov, V. Crystallizing membrane proteins using lipidic mesophases. Nat. Protocols 4, 706–731 (2009).
- Rivara, S., Mor, M., Bedini, A., Spadoni, G. & Tarzia, G. Melatonin receptor agonists: SAR and applications to the treatment of sleep-wake disorders. *Curr. Top. Med. Chem.* 8, 954–968 (2008).
- Bento, A. P. et al. The ChEMBL bioactivity database: an update. Nucleic Acids Res. 42, D1083–D1090 (2014).

- Nonno, R. et al. A new melatonin receptor ligand with mt1-agonist and MT2-antagonist properties. J. Pineal Res. 29, 234–240 (2000).
- Zlotos, D. P., Jockers, R., Cecon, E., Rivara, S. & Witt-Enderby, P. A. MT1 and MT2 melatonin receptors: ligands, models, oligomers, and therapeutic potential. *J. Med. Chem.* 57, 3161–3185 (2014).
- Teh, M. T. & Sugden, D. Comparison of the structure-activity relationships of melatonin receptor agonists and antagonists: lengthening the N-acyl side-chain has differing effects on potency on *Xenopus* melanophores. *Naunyn Schmiedebergs Arch. Pharmacol.* 358, 522–528 (1998).
- Valentin-Hansen, L. et al. The arginine of the DRY motif in transmembrane segment III functions as a balancing micro-switch in the activation of the β2-adrenergic receptor. J. Biol. Chem. 287, 31973–31982 (2012).
- Spadoni, G. et al. Highly potent and selective MT2 melatonin receptor full agonists from conformational analysis of 1-benzyl-2-acylaminomethyltetrahydroguinolines. J. Med. Chem. 58, 7512–7525 (2015).

Acknowledgements We thank M. Chu, C. Hanson, K. Villers, and J. Velasquez for help with cloning and expression, T. Grant for XFEL data processing, and H. Shaye for technical support. This work was supported by the National Institutes of Health grants R35 GM127086 (V.C.), R21 DA042298 (W.L.), R01 GM124152 (W.L.), U24DK116195 (B.L.R.), R01MH112205 (B.L.R.), the NIMH Psychoactive Drug Screening Program and the Michael Hooker Distinguished Professorship to B.L.R. and F31-NS093917 (R.H.J.O.), the STC Program of the National Science Foundation (NSF) through BioXFEL (No. 1231306) (B.S., U.W., W.L., N.A.Z., V.C.), NSF ABI grant 1565180 (C.L., N.Z., U.W.), HFSP long-term fellowship LT000046/2014-L (L.C.J.), postdoctoral fellowship from the Swedish Research Council (L.C.J.) and EMBO ALTF 677-2014 (B.S.). Parts of this research were carried out at the LCLS, a National User Facility operated by Stanford University on behalf of the US Department of Energy and supported by the US Department of Energy Office of Science, Office of Basic Energy Sciences under Contract No. DE-AC02-76SF00515. This research benefited from the use of credits from the National Institutes of Health (NIH) Cloud Credits Model Pilot, a component of the NIH Big Data to Knowledge (BD2K) program.

Reviewer information *Nature* thanks Christian Siebold, leva Sutkeviciute, Jean-Pierre Vilardaga and the other anonymous reviewer(s) for their contribution to the peer review of this work.

Author contributions L.C.J., B.S., V.K., and V.C. conceived the project, analysed data, and wrote the paper with contributions from all authors. L.C.J. and B.S. designed, optimized, purified and characterized receptor constructs for structural studies and crystallized the receptor, prepared crystal samples and figures, solved and refined the structures, and assisted in generating mutant constructs for binding and functional analyses. J.D.M., X.-P.H., and S.T.S. performed radioligand binding and functional experiments, assisted in making mutant and wild-type constructs, and analysed binding and functional data. L.C.J., B.S., A.B., L.Z., W.L., and V.C. collected XFEL data. S.Z. and U.W. operated the LCP injector during XFEL data collection. S.H., L.Z., and W.L. assisted in XFEL sample preparation. A.B., C.G., C.L., and N.A.Z. processed XFEL data. L.C.J., G.W.H. and A.B. determined the structures. L.C.J. and G.W.H. performed the structure refinement and quality control. N.P., J.M.G., and V.K. designed mutants for radioligand and functional studies, and performed molecular docking and molecular dynamics simulations. R.H.J.O. and A.R.T. assisted with molecular biology and functional experiments. S.Y. synthesized the bitopic compound, analysed data, and edited the paper. R.C.S. contributed to study design and selection of chemical compounds for receptor stabilization and functional characterization, supervised protein expression, and edited the paper. B.L.R. supervised pharmacological experiments and edited the paper. V.K. supervised molecular docking and molecular dynamics calculations. V.C. coordinated and supervised the whole project.

Competing interests The authors declare no competing interests.

Additional information

Extended data is available for this paper at https://doi.org/10.1038/s41586-019-1144-0.

 $\label{lem:supplementary information} \textbf{Supplementary information} \ is available for this paper at \ https://doi.org/10.1038/s41586-019-1144-0.$

Reprints and permissions information is available at http://www.nature.com/reprints.

Correspondence and requests for materials should be addressed to B.L.R., V.K. or V.C.

Publisher's note: Springer Nature remains neutral with regard to jurisdictional claims in published maps and institutional affiliations.

© The Author(s), under exclusive licence to Springer Nature Limited 2019

METHODS

No statistical methods were used to predetermine sample size. The experiments were not randomized and the investigators were not blinded to allocation during experiments and outcome assessment.

Design and expression of MT_2 crystallized construct. The DNA sequence of human MT₂ receptor (UniProt²¹ identifier P49286) was synthesized by GenScript with optimization for expression in insect cells. The crystallized construct (MT₂-CC) has truncations of N-terminal residues 1–30 and C-terminal residues 341-362. The thermostabilized apocytochrome BRIL (UniProt P0ABE7) from Escherichia coli with mutations M7W, H102I and R106L was fused to the truncated N terminus of MT2 with a six-residue linker (GDGARP). Another fusion protein, rubredoxin (Rub, UniProt P00268), was fused in ICL3, replacing receptor residues 232-240. For construct optimization (to increase monodispersity, thermostability and crystallizability), the following point mutations were added: D86^{2.50}N⁹, L108^{ECL1}F, F129^{3.41}W¹⁰, N137^{3.49}D, C140^{3.52}L, W264^{6.48}F, A305^{7.50}P and N312^{8.47}D (see the accompanying paper⁸ for details). The MT₂-CC coding sequence was subcloned into a modified pFastBac1 (Invitrogen) vector, with a haemagglutinin (HA) signal sequence and a Flag tag on the N terminus and a PreScission protease cleavage site followed by a 10× His tag on the C terminus. The receptor was expressed in Spodoptera frugiperda cells (Sf9, purchased from ATCC, CRL-1711, authenticated by supplier using morphology and growth characteristics, certified mycoplasma-free), which were collected and stored as described in the accompanying paper8.

Purification of MT₂-CC. Insect cell membranes were prepared by thawing frozen cell pellets in a hypotonic buffer containing 10 mM HEPES (pH 7.5), 10 mM MgCl₂, 20 mM KCl, and homemade protease inhibitor cocktail. Extensive washing of the raw membranes was performed by repeated Dounce homogenization and centrifugation in hypotonic buffer (once), followed by high osmotic buffer containing 1.0 M NaCl, 10 mM HEPES (pH 7.5), 10 mM MgCl₂, 20 mM KCl, and homemade protease inhibitor cocktail (two or three times), thereby separating soluble and membrane-associated proteins from integral membrane proteins. Stocks (100 mM) of 2-PMT (Tocris) and ramelteon (Apex Biosciences) were dissolved in DMSO. Washed membranes were resuspended into a buffer containing $50\,\mu M$ 2-PMT or ramelteon, 2 mg ml⁻¹ iodoacetamide, and homemade protease inhibitor cocktail, and incubated at 4°C for 30 min before solubilization. The membranes were then solubilized in 50 mM HEPES (pH 7.5), 150 mM NaCl, 1% (wt/vol) n-dodecyl-β-D-maltopyranoside (DDM, Anatrace), 0.2% (wt/vol) cholesteryl hemisuccinate (CHS, Sigma-Aldrich) at 4°C for 3 h. The supernatant was isolated by centrifugation at 60,000g for 50 min, and incubated in 20 mM HEPES (pH 7.5), 800 mM NaCl with Talon (immobilized metal affinity chromatography IMAC) resin (Clontech) overnight at $4\,^{\circ}\text{C}.$ After binding, the resin was washed with twenty column volumes of wash buffer 1 (50 mM HEPES (pH 7.5), 50 µM 2-PMT or ramelteon, 800 mM NaCl, 10% (vol/vol) glycerol, 0.1% (wt/vol) DDM, 0.02% (wt/vol) CHS, 10 mM imidazole), followed by ten column volumes of wash buffer 2 (50 mM HEPES (pH 7.5), 50 μM 2-PMT or ramelteon, 150 mM NaCl, 10% (vol/vol) glycerol, 0.05% (wt/vol) DDM, 0.01% (wt/vol) CHS, 50 mM imidazole). The protein was then eluted in minimal volumes of elution buffer (50 mM HEPES (pH 7.5), $50\,\mu\text{M}$ 2-PMT or ramelteon, $150\,\text{mM}$ NaCl, 10% (vol/vol) glycerol, 0.02% (wt/vol) DDM, 0.01% (wt/vol) CHS, 220 mM imidazole). PD MiniTrap G-25 columns (GE Healthcare) were used to remove imidazole. The protein was then treated overnight with His-tagged PreScission protease (GenScript) to cleave the C-terminal His-tag. PreScission protease and the cleaved C-terminal fragment were removed by binding to Talon IMAC resin for 1.5 h at 4 °C. The protein was collected as the TALON IMAC column flow-through. The ligand concentration was increased to 100 μM, and the protein was concentrated to 30–40 mg ml⁻¹ with a 100-kDa molecular mass cut-off Vivaspin centrifuge concentrator (Sartorius).

Protein stability assays. The stability of purified MT₂-CC was analysed using a microscale thermostability assay²² using Rotorgene (QIAGEN). In brief, 1–5 µg of protein was mixed with 1.5 µM 7-diethylamino-3-(4'-maleimidylphenyl)-4-methylcoumarin (CPM) dye (2.5 mM stock in DMSO) in 25 mM HEPES pH 7.5, 150 mM NaCl, 0.02% DDM (wt/vol), 0.004% CHS (wt/vol), 10% glycerol (vol/vol), and indicated concentrations of compounds to a final volume of 100 µl. Samples were incubated for 15 min at 20 °C and then heated gradually from 25 °C to 95 °C at a rate of 2 °C min⁻¹, monitoring CPM fluorescence (excitation 365 nm, emission 460 nm). The melting temperature ($T_{\rm m}$) was determined using the derivative of the resulting melting temperature curve after background subtraction using Prism 7.0 (GraphPad).

Crystallization. Purified $\mathrm{MT_2}\text{-CC}$ in complex with 2-PMT or ramelteon was reconstituted into LCP by mixing it with molten lipid using a mechanical syringe mixer¹³. The protein–LCP mixture contained 40% (wt/wt) receptor solution, 54% (wt/wt) monoolein, and 6% (wt/wt) cholesterol. Crystallization trials were performed in 96-well glass sandwich plates (Marienfeld) using an NT8-LCP robot (Formulatrix) by dispensing 40 nl of protein-laden LCP and 800 nl of precipitant solution per well. Plates were incubated and imaged at 20 °C using an automatic

incubator/imager (RockImager 1000, Formulatrix). Initial crystal hits were identified in a condition containing 100 mM HEPES, pH 6.8, 30% (vol/vol) PEG 400, 100 mM NH₄CH₃CO₂. These crystals, approximately $30 \times 30 \times 70 \,\mu\text{m}^3$, were collected using micromounts (MiTeGen) and flash-frozen in liquid nitrogen for data collection at a microfocus synchrotron source. After extensive optimization, the best crystals diffracted to about 3.0 Å resolution, but suffered from radiation damage, resulting in a 3.5 Å complete dataset. Additives had no effect on diffraction quality. Microcrystals for SFX data collection were prepared in gas-tight syringes (Hamilton) as previously described²³. After optimization, diffraction-quality crystals were obtained from 100 mM ADA pH 5.8-6.5, 24-28% (vol/vol) PEG 400, 10–200 mM NH₄CH₃CO₂, 50 μM 2-PMT or ramelteon, by injecting 5 μl of proteinladen LCP into $50 \,\mu l$ precipitant in syringes. Before loading the microcrystals into the LCP injector, excess precipitant was removed and 7.9 monoacylglycerol (MAG) lipid was added to the LCP to absorb any residual precipitant solution and to prevent crystalline phase formation upon rapid cooling when injecting LCP into vacuum²⁴.

Crystallographic data collection. Data collection was performed at the Coherent X-ray Imaging (CXI)²⁵ end station of the Linac Coherent Light Source (LCLS), which operated at a wavelength of 1.3 Å (9.83 keV) delivering individual X-ray pulses of 30 and 43 fs pulse duration and approximately 10¹¹ photons per pulse focused into a spot size of approximately 1.5 µm in diameter using a pair of Kirkpatrick-Baez mirrors. Microcrystals (Extended Data Fig. 1c) of MT₂ (approximately $5 \times 5 \times 5 \mu m^3$) were delivered in the LCP medium using an LCP microextrusion injector²⁴ with 50-μm nozzle running at a flow rate of approximately 300 nl min⁻¹. Diffraction images were recorded at a rate of 7,200 patterns per minute (120 Hz) with the 2.3 Megapixel Cornell-SLAC Pixel Array Detector (CSPAD)²⁶. Initial diffraction frames were corrected and filtered using the software package Cheetah²⁷. A crystal 'hit' was defined as an image containing a minimum of 20 diffraction peaks with a signal-to-noise ratio above 4 and a number of pixels above 3. After further refinement of parameters (peak detection, prediction and integration), images were indexed using MOSFLM²⁸, DirAx²⁹, and XDS³⁰ and integrated and merged into a final dataset using CrystFEL v.0.6.2 software suite³¹. Integration radii of 3, 5, and 6 pixels with per pattern resolution cut-offs 1.0 nm⁻¹ above the conservative resolution estimates for each crystal were applied (push-res option), otherwise default values were used. The total numbers of collected images/hits/indexed images are as follows: 2,154,963/84,928/31,677 (MT₂-CC-2-PMT), 476,863/59,071/28,130 $(\mathrm{MT_2\text{-}CC(H208A)} - 2\text{-}\mathrm{PMT}), 293,060/22,267/20,704 \ (\mathrm{MT_2\text{-}CC(N86D)} - 2\text{-}\mathrm{PMT}),$ 727,004/60,005/28,834 (MT₂-CC-ramelteon). As a resolution cutoff, the criterion³² of CC*>0.5 was used for all datasets (see Extended Data Table 2 for data statistics). The space group was determined to be $P2_1$, with two molecules per asymmetric unit.

Structure determination. To solve the 2.8 Å resolution MT₂-CC-2-PMT structure, a search model was generated as follows: the MT2 receptor sequence was sent to the HHpred server³³, and the output models were reduced by removing all low-resolution (<3.0 Å) and NMR structures. The RCSB Protein Data Bank (PDB) files of the top ten hits were downloaded and prepared with Sculptor³⁴. The models were structurally superimposed, and the side chains were pruned, yielding the conserved receptor core model. The model that produced a successful molecular replacement solution with Phaser³⁵ (TFZ score of 14.9 and LLG of 320) was based on the C-C chemokine receptor 2 structure (PDB ID: 5T1A)³⁶. This solution containing two receptor molecules was fixed as a partial solution, and the search continued with rubredoxin (PDB ID: 1IRO), in which one molecule was placed in the asymmetric unit. The resulting three-component solution was subjected to several rounds of refining with phenix.refine³⁷ and model building with phenix.autobuild³⁸ followed by manual refinement in Coot³⁹. BRIL (PDB ID: 1M6T) was then used independently as a search model for remaining fusion partners in the asymmetric unit. The second BRIL was manually modelled into the electron density; however, no density could be found for the second rubredoxin molecule, which, therefore, was not modelled in the final structure. This rubredoxin fusion partner is likely to be disordered and does not participate in crystal contacts, however, there is space for it in the crystal lattice (Extended Data Fig. 1d). A zinc ion was modelled in rubredoxin as previously described⁴⁰. Refinement and model completion were performed by repetitive cycling between Refmac541 or autoBUSTER v.2.10.2⁴² and manual rebuilding in Coot³⁹ using both $2mF_0 - DF_c$ and $mF_0 - DF_c$ maps. Ligand restraints for refinement of 2-PMT and ramelteon coordinates were generated by Prodrg⁴³. For the other three datasets, the MT₂-CC-2-PMT structure was used as a search model for molecular replacement, and the refinement procedure was repeated as described above. The Ramachandran plot obtained by MolProbity⁴⁴ shows that, with the exception of Y92 from the YPYP motif, all residues are in the favoured/allowed regions: 95.4/4.4% of residues (MT₂-CC-2-PMT), 93/6.8% of residues (MT₂-CC(H208A)-2-PMT), 94.8/5.0% of residues (MT₂-CC(N86D)-2-PMT), 95.3/4.5% of residues (MT₂-CC-ramelteon). Data collection and refinement statistics are summarized for each structure in



Extended Data Table 2. Figures containing electron density and molecular structures were generated using PyMol⁴⁵.

Channel profile calculations. The channel diameter profile along its length was calculated with CAVER analyst v.2.0⁴⁶ using default parameters. Further details can be found in the accompanying paper⁸.

Molecular docking. MT_2 receptor ligands obtained from the ChEMBL database¹⁵ were docked into the 2-PMT-bound crystal structures using an energy based docking in ICM-Pro v3.8-6⁴⁷ as described in the accompanying paper⁸.

Molecular dynamics simulations. The experimental structure of MT_2 was prepared and subjected to molecular dynamics simulations as described in the accompanying paper⁸. The simulation periodic box had dimensions (x, y, z) of 75.5 Å, 75.5 Å, 105.4 Å, and contained lipids (129 POPC molecules), 10,281 water molecules, 26 sodium ions, and 36 chloride ions.

Radioligand binding assays. Equilibrium binding assays were performed and analysed as described in the accompanying paper 8 . HEK293T cells were obtained from ATCC (CRL-11268, authenticated by supplier using morphology, growth characteristics and short tandem repeat profiling, certified mycoplasma-free). For kinetic studies, to initiate dissociation of $[^3\mathrm{H}]$ melatonin, $10~\mu\mathrm{l}$ of cold excess melatonin ($10~\mu\mathrm{M})$ was added per well at specific time points ranging from 2 min to 10 h, and immediately at time = 0 min plates were collected. Dissociation experiments were performed at 25 °C for MT $_1$ and 37 °C for MT $_2$ because of the slow kinetics in MT $_2$. For all assays, non-specific activity was defined by the addition of 5 $\mu\mathrm{M}$ 2-PMT. Ligand dissociation data were analysed using 'Dissociation-One phase exponential decay' to yield estimates of $k_{\rm off}$ using GraphPad Prism 7.0.

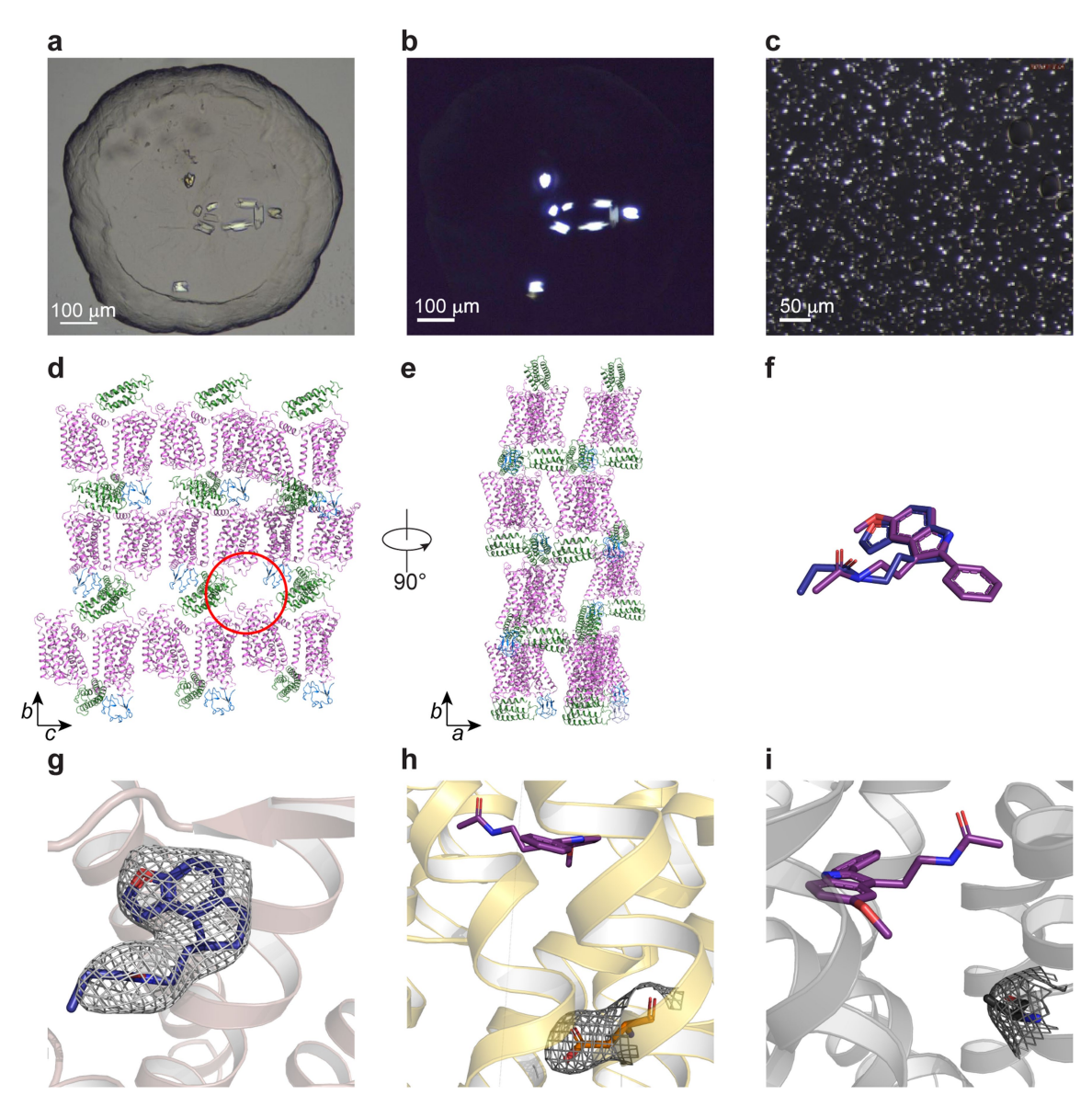
 MT_2 $G_{i/o}$ -mediated cAMP inhibition assay. MT_2 $G_{i/o}$ -mediated cAMP inhibition assays were performed in HEK293T cells as described in the accompanying paper⁸. **Reporting summary.** Further information on research design is available in the Nature Research Reporting Summary linked to this paper.

Data availability

Structure factors and coordinates were deposited in the Protein Data Bank under the following accession codes: $6ME6\ (MT_2-CC-2-PMT)$, $6ME7\ (MT_2-CC(H208A)-2-PMT)$, $6ME8\ (MT_2-CC(N86D)-2-PMT)$, $6ME9\ (MT_2-CC-ramelteon)$.

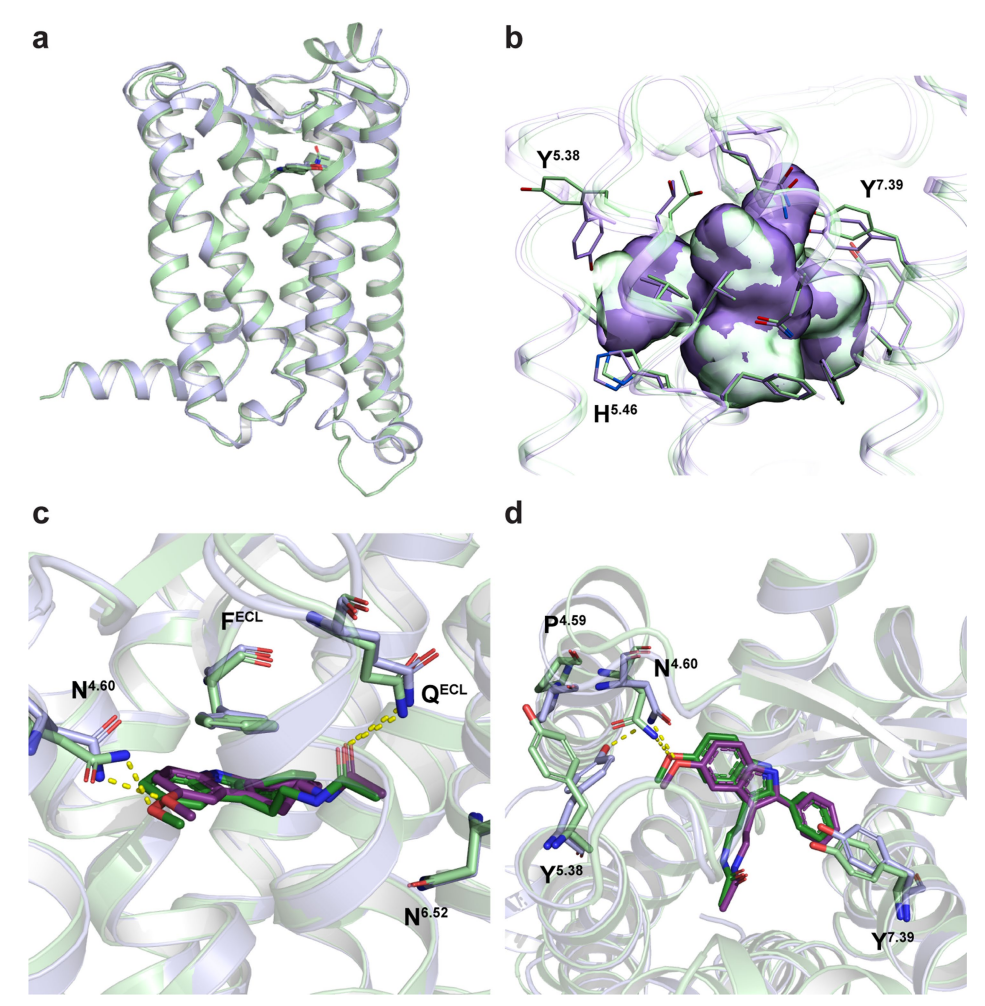
- 21. UniProt Consortium, T. UniProt: the universal protein knowledgebase. *Nucleic Acids Res.* **46**, 2699 (2018).
- Alexandrov, A. I., Mileni, M., Chien, E. Y., Hanson, M. A. & Stevens, R. C. Microscale fluorescent thermal stability assay for membrane proteins. *Structure* 16, 351–359 (2008).
- 23. Liu, W. et al. Serial femtosecond crystallography of G protein-coupled receptors. *Science* **342**, 1521–1524 (2013).
- Weierstall, U. et al. Lipidic cubic phase injector facilitates membrane protein serial femtosecond crystallography. Nat. Commun. 5, 3309 (2014).

- Boutet, S. W. G. J. The Coherent X-ray Imaging (CXI) instrument at the Linac Coherent Light Source (LCLS). New J. Phys. 12, 035024 (2010).
- Hart, P. et al. The CSPAD Megapixel X-ray Camera at LCLS. In X-ray Free-electron Lasers: Beam Diagnostics, Beamline Instrumentation and Applications (eds. S. P. Moeller, S. P. et al.) 85040C–85012 (2012).
- Barty, A. et al. Cheetah: software for high-throughput reduction and analysis of serial femtosecond X-ray diffraction data. J. Appl. Crystallogr. 47, 1118–1131 (2014).
- Battye, T. G., Kontogiannis, L., Johnson, O., Powell, H. R. & Leslie, A. G. iMOSFLM: a new graphical interface for diffraction-image processing with MOSFLM. Acta Crystallogr. D 67, 271–281 (2011).
- Duisenberg, A. J. M. Indexing in single-crystal diffractometry with an obstinate list of reflections. J. Appl. Crystallogr. 25, 92–96 (1992).
- 30. Kabsch, W. Xds. Acta Crystallogr. D 66, 125–132 (2010)
- White, T. A. et al. Recent developments in CrystFEL. J. Appl. Crystallogr. 49, 680–689 (2016).
- 32. Karplus, P. A. & Diederichs, K. Linking crystallographic model and data quality. *Science* **336**, 1030–1033 (2012).
- Zimmermann, L. et al. A completely reimplemented MPI bioinformatics toolkit with a new HHpred server at its core. J. Mol. Biol. 430, 2237–2243 (2018).
- Bunkóczi, G. & Read, R. J. Improvement of molecular-replacement models with Sculptor. Acta Crystallogr. D 67, 303–312 (2011).
- McCoy, A. J. et al. Phaser crystallographic software. J. Appl. Crystallogr. 40, 658–674 (2007).
- Zheng, Y. et al. Structure of CC chemokine receptor 2 with orthosteric and allosteric antagonists. *Nature* 540, 458–461 (2016).
- 37. Afonine, P. V. et al. Towards automated crystallographic structure refinement with phenix.refine. *Acta Crystallogr. D* **68**, 352–367 (2012).
- Adams, P. D. et al. PHENIX: a comprehensive Python-based system for macromolecular structure solution. Acta Crystallogr. D 66, 213–221 (2010).
- Emsley, P., Lohkamp, B., Scott, W. G. & Cowtan, K. Features and development of Coot. Acta Crystallogr. D 66, 486–501 (2010).
- Tan, Q. et al. Structure of the CCR5 chemokine receptor–HIV entry inhibitor maraviroc complex. Science 341, 1387–1390 (2013).
- Murshudov, G. N., Vagin, A. A. & Dodson, E. J. Refinement of macromolecular structures by the maximum-likelihood method. *Acta Crystallogr. D* 53, 240–255 (1997).
- 42. BUSTÉR v. 2.10.2.
- Schüttelkopf, A. W. & van Aalten, D. M. PRODRG: a tool for high-throughput crystallography of protein–ligand complexes. Acta Crystallogr. D 60, 1355–1363 (2004).
- 44. Chen, V. B. et al. MolProbity: all-atom structure validation for macromolecular crystallography. *Acta Crystallogr. D* **66**, 12–21 (2010).
- 45. The PyMOL Molecular Graphics System. Version 2.0 Schrödinger, LLC.
- Jurcik, A. et al. CAVER Analyst 2.0: analysis and visualization of channels and tunnels in protein structures and molecular dynamics trajectories. *Bioinformatics* 34, 3586–3588 (2018).
- Abagyan, R. A., Totrov, M. M. & Kuznetsov, D. A. ICM: a new method for protein modeling and design: applications to docking and structure prediction from the distorted native conformation. *J. Comput. Chem.* 15, 488–506 (1994).



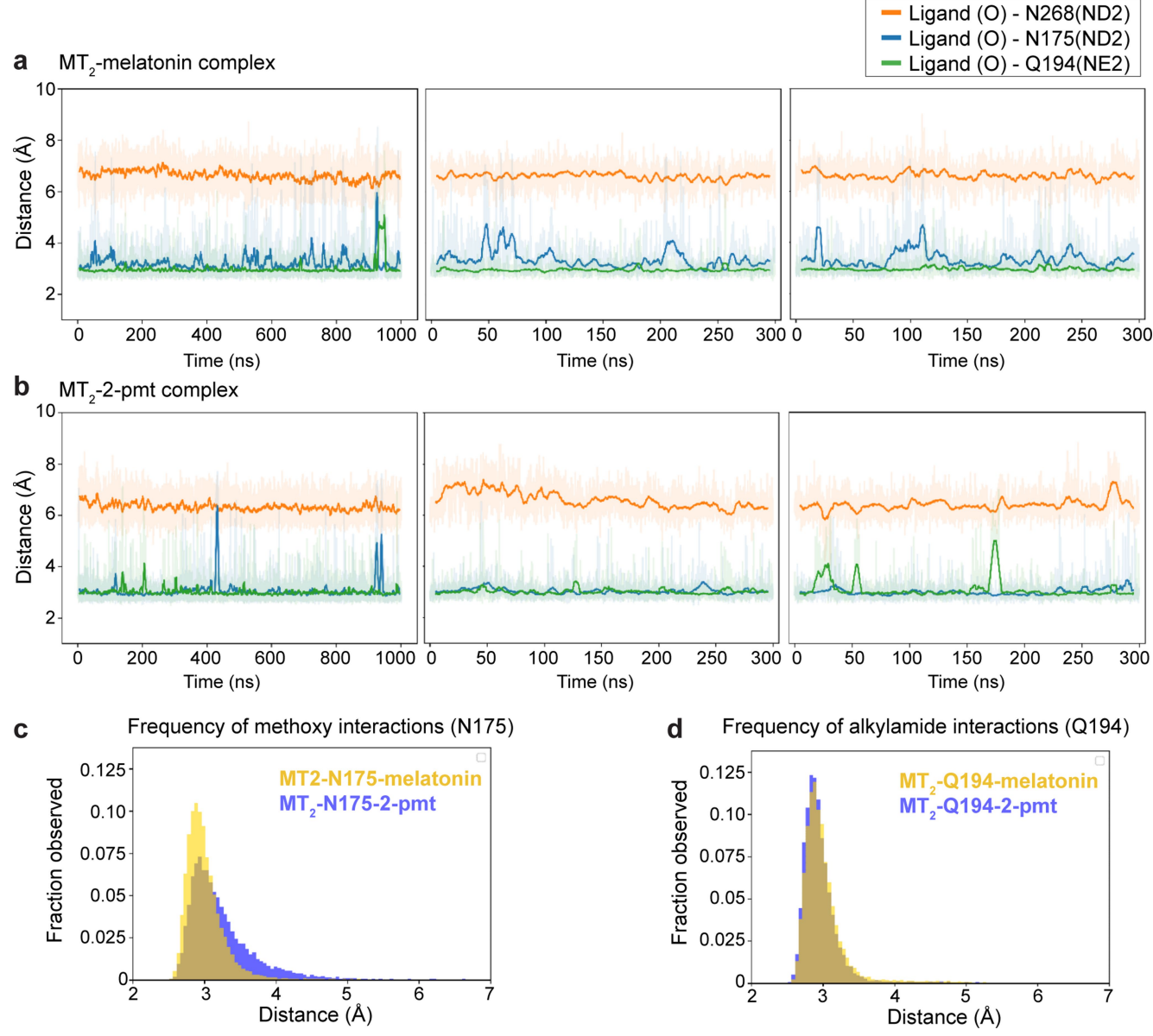
Extended Data Fig. 1 | Crystallization of MT₂: crystals, crystal packing and electron density. a, b, Bright field (a) and cross-polarized images (b) of representative MT₂–2-PMT crystals optimized for synchrotron data collection (representing three independent crystallization setups). c, Cross-polarized image of representative MT₂(N86D)–2-PMT crystals used for XFEL data collection (representing three independent crystallization setups). See Extended Data Table 2 for data collection

statistics. **d**, **e**, Crystal packing (receptor, purple; BRIL, green; rubredoxin, blue). Space for missing rubredoxin in molecule B of the asymmetric unit is indicated with a red circle. Lattice rotated 90° is shown in **e**. **f**, Overlay of 2-PMT (purple) and ramelteon (blue) ligands of MT₂. **g–i**, $2mF_0 - DF_c$ density (grey) contoured at 1σ of ramelteon (**g**), N86^{2.50}D mutation (**h**), and H208^{5.46}A mutation (**i**). 2-PMT is shown in purple.



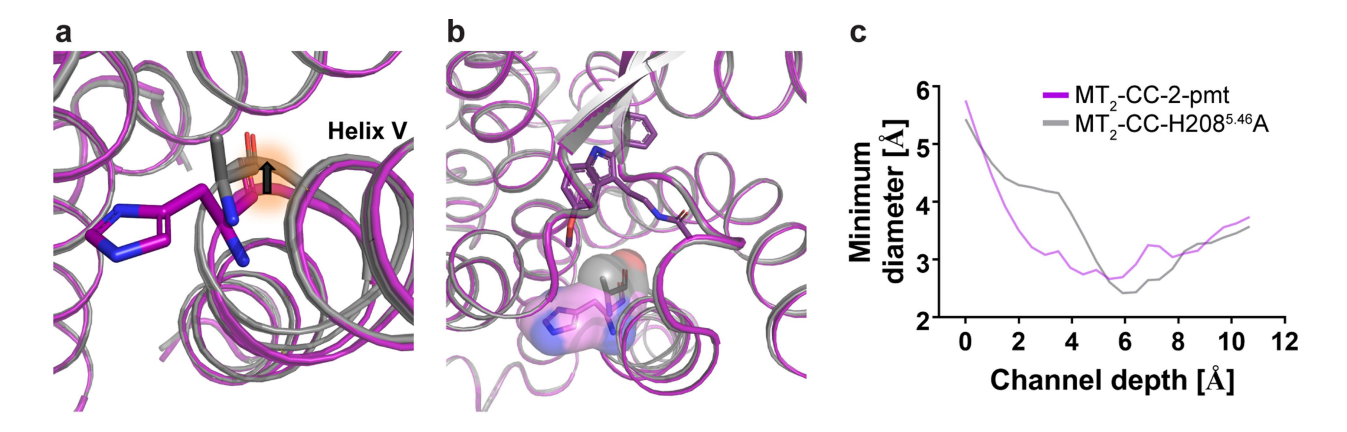
Extended Data Fig. 2 | Structural differences between MT₁ and MT₂. a, Overlay of MT₁–2-PMT (green) and MT₂–2-PMT (violet) structures ($C\alpha$ r.m.s.d = 0.6 Å). b, Comparison of MT₁ (green) and MT₂ (violet) binding pockets. Overall, the binding pocket in MT₂ is about 50 ų larger than in MT₁. c, Comparison of 2-PMT ligand conformations in

 MT_1 (green) and MT_2 (violet). Hydrogen bonds are shown as yellow dashed lines. $\boldsymbol{d},$ Overlay of MT_1 and $MT_2,$ showing residues with different conformations in the vicinity of the binding pocket. $N^{4.60}$ makes a hydrogen bond with $Y^{5.38}$ in MT_2 but not in $MT_1.$



Extended Data Fig. 3 | Molecular dynamics simulations. a, b, Distance plots for interactions between residues in MT $_2$ (N175 $^{4.60}$, atom ND2; Q194 ECL2 , atom NE2; N268 $^{6.52}$, atom ND2), and closest oxygen atoms of the ligand methoxy and acetyl groups, respectively, in complexes with melatonin (a) and 2-PMT (b) from three independent simulation

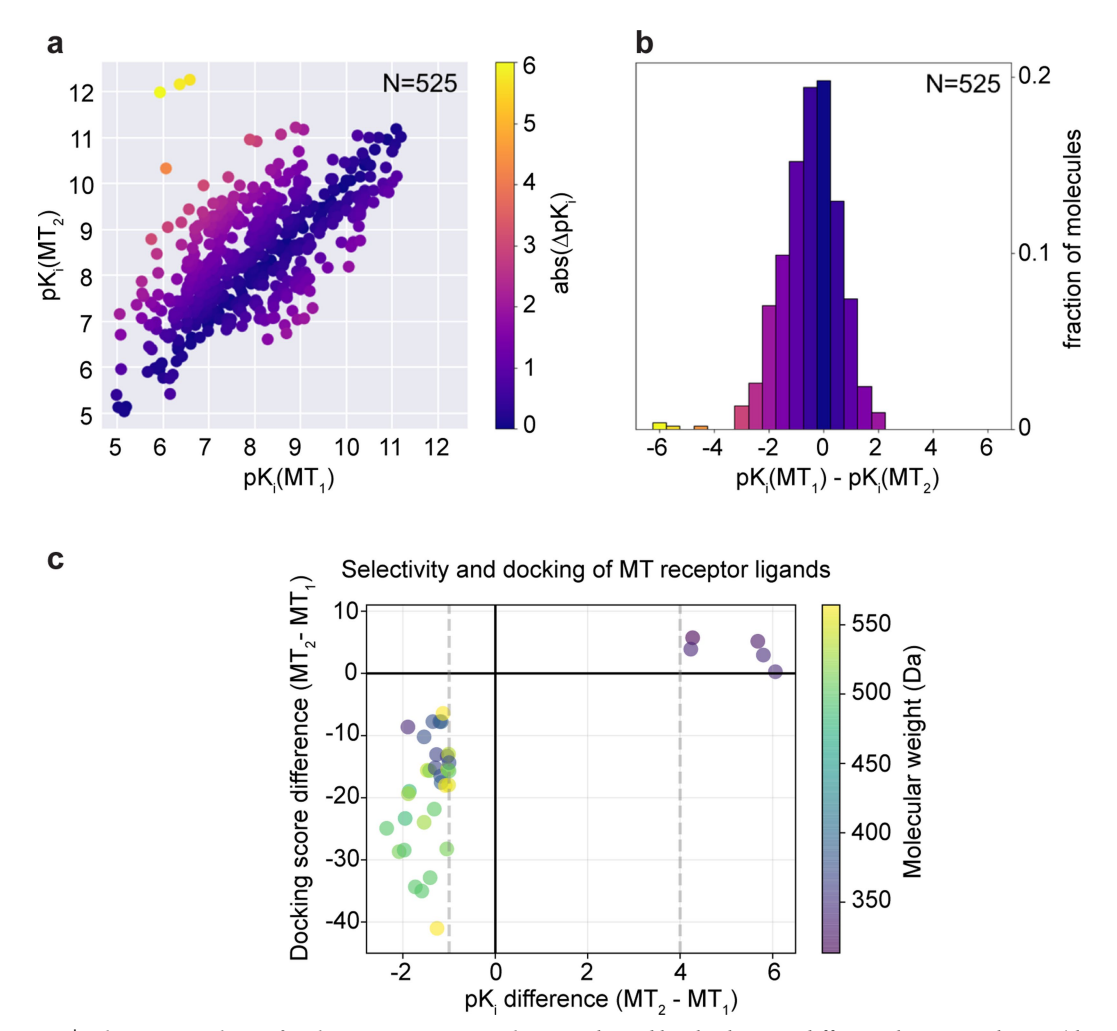
runs. **c**, Distance histograms for interactions of N175^{4.60} with methoxy of melatonin (yellow) and 2-PMT (violet). **d**, Distance histograms for interactions of Q194^{ECL2} with alkylamide tail of melatonin (yellow) and 2-PMT (violet).



		melatonin		C.	TL 01-05-B-A0	5
Mutant	EC ₅₀ , nM [n] (pEC ₅₀ ± s.e.m.)	%E _{MAX} (%E _{MAX} *)	$\Delta ext{log(E}_{ ext{MAX}} / \\ ext{EC}_{50}) \\ ext{(mutant-wt)}$	$\begin{array}{c} EC_{50},nM\;[n]\\ (pEC_{50}^{}\!\pm s.e.m.) \end{array}$	%E _{MAX} (%E _{MAX} *)	$\Delta log(E_{MAX}/EC_{50})$ (mutant-wt)
WT	0.028 [16] (10.56±0.09)	100 (100)	0	16.59 [6] (7.78±0.07)	100 (63±7)	0
H208A (5.46)	0.190 [9] (9.72±0.26)	80±9	-0.93	No	agonist activit	у

Extended Data Fig. 4 | Structural and functional differences between MT₂–2-PMT and MT₂(H208A^{5.46})–2-PMT. a, Overlay of the MT₂–2-PMT (purple) structure with that of MT₂(H208^{5.46}A)–2-PMT (grey) reveals an inward shift of helix V of about 0.9 Å, due to the H208^{5.46}A mutation (black arrow). b, Surface representation of the H208^{5.46} and H208^{5.46}A residues. Rotation of helix V renders the binding pocket volume about 50 ų smaller for the H208^{5.46}A structure (binding site volume for MT₂–2-PMT: 766 ų compared to 716 ų for the MT₂(H208^{5.46}A)–2-PMT structure). c, Comparison of the channel profiles (from the outside of the protein towards the ligand) for

 $\rm MT_2-2\text{-}PMT$ (purple) and $\rm MT_2(H208^{5.46}A)-2\text{-}PMT$ (grey) reveals a narrowing of the $\rm MT_2(H208^{5.46}A)-2\text{-}PMT$ channel at a depth of around 6 Å as a consequence of the mutation and subsequent inward rotation of helix V. **d**, Functional data for wild-type and H208^{5.46}A mutant MT $_2$ expressed in HEK293T cells by using GloSensor to measure $\rm G_{i/o}$ -mediated inhibition of cAMP. Data represent mean \pm s.e.m. for n independent experiments as indicated in square brackets. $\rm \%\it ME_{MAX}$ (maximum effect of a drug) is relative to wild-type receptor (in columns), and $\rm \%\it ME_{MAX}*$ is relative to melatonin activity (in rows). See Methods for further information and Supplementary Fig. 6 for dose–response curves.



Extended Data Fig. 5 | Selectivity analysis of melatonergic compounds. a, Binding affinities of ligands for MT $_1$ (ChEMBL target identifier CHEMBL1945) and MT $_2$ (CHEMBL1946) were retrieved from the ChEMBL database¹⁵ (v. 24) of experimental literature values. Of these ligands, 525 have affinities reported for both receptor subtypes. For ligands with multiple reported affinity values for a given receptor, p K_i values were averaged. MT $_1$ -selective ligands are in the lower right quadrant; MT $_2$ -selective ligands are in the upper left quadrant. Data points are

coloured by absolute pK_i difference between subtypes (that is, selectivity). **b**, Histogram of observed ligand selectivities. MT_2 selective ligands are on the left of the panel, MT_1 selective ligands are on the right. **c**, Plot of the docking score difference of select ligands that were docked between MT_2 and MT_1 versus their pK_i difference ($MT_2 - MT_1$). Dashed lines indicate pK_i selectivity cutoff criteria (MT_1 : -1 and MT_2 : 4). Data points are coloured by molecular mass (Da). See Supplementary Table 1 for details of docked ligands.



Extended Data Table 1 \mid Ligand affinity data for MT₂ mutants

	melatonin	2-pmt	ramelteon	agomelatine
Mutant _				
	Kd, nM [n]	Ki, nM [n]	Ki, nM [n]	Ki, nM [n]
	(pK _d ±s.e.m.)	(pK _i ±s.e.m.)	(pK _i ±s.e.m.)	(pK _i ±s.e.m.)
WT	0.54 [10] (9.27±0.12)	0.17 [10] (9.78±0.11)	0.23 [4] (9.66±0.10)	0.24 [4] (9.63±0.08)
WT + NaCl	1.56 [6] (8.81 ± 0.18)	ND	ND	ND
MT ₂ -CC (Sf9)	63.10 [3] (7.20±0.06)	3.14 [4] (8.50±0.06)	2.60 [4] (8.59±0.02)	6.88 [4] (8.16±0.05)
MT ₂ -CC (sf9) + NaCl	48.23 [3] (7.32±0.03)	ND	ND	ND
MT ₂ -CC-N86 ^{2.50} D (Sf9)	29.40 [6] (7.53±0.34)	6.46 [4] (8.19±0.15)	7.37 [4] (8.13±0.09)	26.76 [4] (7.57±0.05)
// ₂ -CC-H208 ^{5.46} A (Sf9)	10.81 [6]	3.57 [6]	2.03 [6]	4.98 [6]
-	(7.97±0.16)	(8.45±0.03)	(8.69±0.13)	(8.30±0.04)
D86N (2.50)	5.80 [3] (8.24±0.04)	0.33 [3] (9.48±0.12)	ND	ND
D86N (2.50) + NaCl	3.26 [3] (8.49±0.09)	ND	ND	ND
L108F (ECL1)	0.94 [3] (9.03±0.11)	0.13 [3] (9.87±0.15)	ND	ND
F129W (3.41)	2.84 [3] (8.55±0.04)	0.22 [3] (9.65±0.08)	ND	ND
N137D (3.49)	1.24 [3] (8.91±0.13)	0.12 [3] (9.92±0.00)	ND	ND
C140L (3.52)	0.21 [3] (9.68±0.05)	0.03 [3] (10.50±0.02)	ND	ND
W264F (6.48)	0.88 [3] (9.06±0.14)	0.06 [3] (10.25±0.26)	ND	ND
A305P (7.50)	3.94 [3] (8.40±0.19)	0.47 [3] (9.32±0.06)	ND	ND
N312D (7.57)	2.85 [3] (8.54±0.07)	0.36 [3] (9.44±0.04)	ND	ND
P95A (2.59)	,	No specific bind	ling up to 7 nM [³H]-melatonin	
M120A (3.32)	0.44 [3] (9.42±0.16)	0.028 [3] (10.7±0.3)	0.055 [3] (10.28±0.09)	0.052 [3] (10.35±0.18)
N175A (4.60)	0.86 [3] (9.2±0.3)	0.09 [3] (10.06±0.06)	0.08 [3] (10.12±0.11)	0.25 [3] (9.60±0.04)
F192A (ECL2)	•	Low expression, no spe	cific binding up to 7 nM [³ H]-mela	atonin
F192I (ECL2)		No specific bind	ling up to 7 nM [³H]-melatonin	
Q194A (ECL2)	0.62 [3] (9.4±0.3)	0.043 [3] (10.38±0.07)	0.051 [3] (10.4±0.2)	0.12 [3] (9.94±0.09)
Y200A (5.38)	0.63 [3] (9.3±0.3)	0.14 [3] (9.86±0.01)	0.19 [3] (9.73±0.03)	0.67 [3] (9.18±0.02)
A203F (5.41)	0.82 [5] (9.09±0.01)	0.12 [5] (9.94±0.06)	0.19 [5] (9.47±0.19)	0.42 [5] (9.37±0.19)
H208A (5.46)	1.24 [3] (8.94±0.13)	0.17 [3] (9.79±0.09)	0.18 [3] (9.77±0.11)	0.22 [3] (9.68±0.11)
N268A (6.52)	0.96 [3] (9.3±0.4)	0.09 [3] (10.08±0.09)	0.12 [3] (9.92±0.05)	0.20 [3] (9.69±0.03)
Y294A (7.39)	1.07 [3] (8.99±0.09)	0.042 [3] (10.38±0.04)	0.049 [3] (10.33±0.09)	0.10 [3] (10.04±0.10)
Y308S (7.53)	()	,	ling up to 7 nM [³H]-melatonin	()

Data were acquired with wild-type (WT) MT $_2$ and mutants expressed in HEK293T cells by radioligand competition binding using [3 H]melatonin to yield K_d or K_l affinity estimates. Data represent mean \pm s.e.m. for n independent experiments as indicated in square brackets. Crystal constructs (CC) were expressed in Sf9 cells. ND, not determined. Binding isotherms are shown in Supplementary Fig. 2. For determining the effect of NaCl, binding assays were performed in the presence of 147 nM NaCl (binding isotherms in Supplementary Fig. 3).



Extended Data Table 2 \mid MT $_2$ Crystallographic data collection and refinement statistics

	MT ₂ -CC	-2-pmt ^a	MT ₂ -CC-H20	8 ^{5.46} A-2-pmt ^b	MT ₂ -CC-N86	6 ^{2.50} D-2-pmt ^c	MT ₂ -CC-r	amelteon ^d
Data collection								
Space group Cell dimensions	P2	2 ₁	P	2 ₁	P:	2 ₁	P2 ₁	
a, b, c (Å)	69.5, 146	5.2. 77.3	69.2, 14	6.2. 77.3	68.7, 14	5.8. 77.0	69.4. 14	5.7, 77.2
α, β, γ (°)	90, 11		90, 10		90, 107		90, 100	
Resolution (Å)	21.99-2.80	(2.88-2.80)	21.99-3.20		22.0-3.10 ((3.23-3.10)	22.0-3.30 (
R _{split}	0.146		0.181		0.189		0.201	
Vol	3.07 (4.02			(0.3)		(0.42)
CC*	0.999	,	0.997	` '	0.997	` '	0.997	` '
Completeness (%)	100 (100 (,	100 (,		(100)
Redundancy	571.2 (196.6		133 (221.1	
Refinement								
Resolution (Å)	21.99	-2.80	21.99-3.20		22.0-3.10		22.0-3.30	
No. reflections	35,1	193	24,439		26,179		22,122	
Rwork/Rfree	0.219/	0.249	0.224	0.250	0.234/	0.262	0.248/	0.270
No. atoms	Α	В	Α	В	Α	В	Α	В
Protein	3,333	2,852	3,343	2,786	3,293	2,752	3,227	2,738
Ligand/Zn ⁺²	23/1	23/0	23/1	23/0	23/1	23/0	19/1	19/0
Lipid and other	0	11	0	12	0	0	0	0
B-factors (Å ²)								
Receptor	116.4	121.0	95.0	99.6	114.2	117.2	114.1	118.2
BRIL	162.3	188.9	143.2	176.4	167.6	208.8	185.3	248.1
Rubredoxin	114.7	n/a	100.3	n/a	116.2	n/a	118.6	n/a
Ligand/Zn ⁺²	101.6/114.7	106.1/n/a	73.3/91.2	88.7/n/a	96.9/112.3	102.1/n/a	94.9/117.7	105.6/n/a
Lipids and other	n/a	138.8	n/a	111.0	n/a	n/a	n/a	n/a
R.m.s. deviations								
Bond lengths (Å)	0.0	09	0.0	10	0.0	0.009		009
Bond angles (°)	0.0	97	1.0	06	0.0	96	0.9	95

Number of crystals used for structure determination: a31,677, b28,130, c20,704 and d28,834. Values in parentheses are for highest-resolution shell.



Extended Data Table 3 \mid Functional data ($G_{i/o}$ GloSensor) for MT_2 crystal construct mutants

		melatonin			2-pmt	
Mutant	EC ₅₀ , nM [n] (pEC ₅₀ ±s.e.m.)	%E _{MAX} (%E _{MAX} *)	$\Delta log(E_{MAX} / EC_{50})$ (mutant-WT)	EC ₅₀ , nM [n] (pEC ₅₀ ±s.e.m.)	% E _{MAX} (%E _{MAX} *)	$\Delta log(E_{MAX} / EC_{50})$ (mutant-WT)
WT	0.028 [16] (10.56±0.09)	100 (100)	0	0.018 [14] (10.75±0.11)	100 (100±5)	0
MT ₂ -CC (Sf9)			No ad	ctivity		
MT ₂ -Rub			No ad	ctivity		
D86N (2.50)	3.951 [3] (8.40±0.34)	80±18 (100)	-2.25	1.995 [3] (8.70±0.11)	101±17 (126±21)	-2.04
L108F (ECL1)	0.029 [5] (10.54±0.10)	72±4 (100)	-0.16	0.011 [6] (10.95±0.19)	80±8 (110±11)	0.11
F129W (3.41)	0.011 [6] (10.95±0.17)	128±9 (100)	+0.50	0.007 [6] (11.16±0.20)	128±7 (99±6)	0.52
N137D (3.49)	0.019 [6] (10.72±0.12)	88±6 (100)	-0.11	0.016 [6] (10.81±0.10)	90±5 (103±5)	0.19
C140L (3.52)	0.072 [7] (10.15±0.16)	90±8 (100)	-0.46	0.035 [6] (10.45±0.16)	89±6 101±4)	-0.34
W264F (6.48)	0.044 [7] (10.36±0.09)	117±6 (100)	-0.13	0.020 [5] (10.70±0.40)	118±8 (101±6)	-0.03
A305P (7.50)	0.141 [7] (9.85±0.16)	129±5 (100)	-0.60	0.073 [5] (10.14±0.26)	143±4 (91±6)	-0.45
N312D (7.57)	`0.069 [5] ´ (10.16±0.15)	135±6 (100)	-0.26	0.041 [3] (10.39±0.18)	138±10 (102±8)	-0.21

Data were acquired with wild-type MT_2 and mutants expressed in HEK293T cells by using GloSensor to measure $G_{I/o}$ -mediated cAMP inhibition via isoproterenol stimulation. Data represent mean \pm s.e.m. for n independent experiments as indicated in square brackets. $\%E_{MAX}$ is relative to wild-type receptor (in columns), and $\%E_{MAX}$ * is relative to melatonin (in rows). Mutant effects were calculated by the change in relative activity or log(E_{MAX}), subtracting wild type from mutant. Dose–response curves are shown in Supplementary Fig. 4.



Extended Data Table 4 \mid Functional data ($G_{i/o}$ GloSensor) for MT $_2$ mutants

	melatonin			nin 2-pmt			ra	ramelteon			agomelatine		
Mutant	EC ₅₀ , nM [n] (pEC ₅₀ ±s.e.m.)	% E _{MAX} (%E _{MAX} *)	$\Delta log(E_{MAX} / EC_{50})$ (mutant- wt)	EC ₅₀ , nM [n] (pEC ₅₀ ±s.e.m.)	% E _{MAX} (%E _{MAX} *)	$\Delta log(E_{MAX} / EC_{50})$ (mutant- wt)	EC ₅₀ , nM [n] (pEC ₅₀ ±s.e.m.)	% E _{MAX} (%E _{MAX} *)	$\Delta log(E_{MAX})$ / EC ₅₀) (mutant- wt)	EC ₅₀ , nM [n] (pEC ₅₀ ±s.e.m.)	% E _{MAX} (%E _{MAX} *)	$\Delta log(E_{MAX} / EC_{50})$ (mutant- wt)	
WT	0.028 [16] (10.56±0.09)	100 (100)	0	0.018 [12] (10.75±0.11)	100 (100±4)	0	0.016 [12] (10.81±0.14)	100 (108±3)	0	0.018 [10] (10.75±0.12)	100 (105±4)	0	
P95A (2.59)	,	,		,	, ,	No ac	tivity	, ,		,	, ,		
A171M (4.56)	0.075 [9] 10.13±0.14	66±9 (100)	-0.61	0.032 [8] 10.49±0.11	62±9 (94±14)	-0.46	0.031 [7] 10.51±0.19	67±9 (90±12)	-0.47	0.025 [6] 10.60±0.16	75±10 (107±15)	-0.27	
N175A (4.60)	0.070 [9] (10.16±0.15)	74±10 (100)	-0.53	0.0192 [8] (10.72±0.12)	67±14 91±19	-0.20	0.010 [7] (11.00±0.21)	72±12 (87±14)	+0.05	0.015 (7] (10.82±0.13)	71±7 (91±10)	0.08	
F192A (ECL2)	99.235 [6] (7.00±0.26)	122±7 (100)	-3.46	4.808 [10] 8.32±0.09	139±3 (114±6)	-2.28	4.799 [9] 8.32±0.04	150±4 (109±3)	-2.31	5.316 [9] 8.27±0.05	145±2 (111±2)	-2.31	
F192I (ECL2)	3.00 [3] (8.52±0.30)	159±4 (100)	-1.83	0.211 [3] (9.68±0.07)	159±3 (100±1)	-0.87	0.571 [3] (9.24±0.16)	169±5 (94±3)	-1.34	2.754 [3] (8.56±0.05)	160±8 (94±5)	-1.98	
Q194A (ECL2)	0.025 [3] (10.60±0.22)	131±4 (100)	+0.16	0.011 [3] (10.96±0.08)	130±3 (99±3)	+0.33	0.006 [3] (11.23±0.10)	130±6 (88±4)	+0.54	0.005 [3] (11.30±0.13)	110±15 (78±10)	+0.59	
Y200A (5.38)	0.517 [3] (9.29±0.32)	161±10 (100)	-1.06	0.009 [3] (11.07±0.08)	158±16 (98±10)	+0.53	0.014 [3] (10.86±0.07)	164±21 (90±10)	0.26	0.314 [3] (9.50±0.31)	149±14 (87±8)	-1.07	
H208A (5.46)	0.190 [9] (9.72±0.26)	80±9 (100)	-0.93	0.101 [10] (10.00±0.15)	75±9 (93±11)	-0.88	0.035 [8] (10.45±0.28)	79±11 (88±12)	-0.46	0.083 [8] (10.08±0.26)	76±2 (89±3)	-0.79	
N268A (6.52)	0.046 [3] (10.33±0.27)	141±10 (100)	-0.08	0.013 [3] (10.87±0.10)	140±8 (99±6)	+0.28	0.009 [3] (11.05±0.10)	132±9 (83±6)	+0.36	0.007 [3] (11.16±0.10)	112±4 (75±3)	+0.46	
Q194A (ECL2)/ N268A (6.52)	2.405 [9] 8.62±0.21	116±7 (100)	-1.88	0.033 [10] 10.49±0.18	112±6 (96±5)	-0.21	0.136 [9] 9.87±0.15	121±7 (93±5)	-0.86	0.759 [8] 9.12±0.14	116±4 (94±4)	-1.56	
Y294A (7.39)	0.460 [4] (9.34±0.15)	148±6 (100)	-1.05	0.008 [4] (11.12±0.11)	153±7 (94±9)	+0.56	0.008 [3] (11.11±0.09)	153±11 (114±11)	+0.48	0.015 [3] (10.83±0.20)	118±11 (143±12)	-0.15	
Y308S (7.53)						No ac	tivity						

Data were acquired with MT $_2$ mutants by using GloSensor to measure $G_{I/o}$ -mediated cAMP inhibition via isoproterenol stimulation. Data represent mean \pm s.e.m. for n independent experiments as indicated in square brackets. $K_{E_{MAX}}$ is relative to wild-type receptor (in columns), and $K_{E_{MAX}}$ is relative to melatonin (in rows). Mutant effects were calculated by the change in relative activity, or $\log(E_{MAX}/E_{C_{50}})$ subtracting wild-type from mutant. ND, not determined. Dose–response curves are shown in Supplementary Fig. 5.



Extended Data Table 5 | Thermostability data for MT₂ mutants

Mutant	apo Tm, °C	mlt Tm, °C	2-pmt Tm, °C	mlt ΔTm, °C	2-pmt ΔTm, °C
MT ₂ -CC	63.6±0.3	73.4±0.1	79.9±0.4	+9.8	+16.3
W129F (3.41)	59.0±0.2	72.4±0.1	78.9±0.3	+13.4	+19.9
N175A (4.60)	64.6±0.3	70.6±0.1	78.1±0.2	+6	+13.5
F192A (ECL2)	57.1±0.5	66.5±0.1	75.4±0.1	+9.4	+18.3
Q194A (ECL2)	65.5±0.3	69.9±0.3	77.3±0.2	+4.4	+11.8
H208A (5.46)	58.7±0.6	72.6±0.4	78.9±0.3	+13.9	+20.2
N268A (6.52)	63.3±0.3	66.1±0.2	74.6±0.3	+2.8	+11.3
Q194A (ECL2)/N268A (6.52)	67.9±0.3	67.9±0.1	71.4±0.3	0	+3.5
Y308S (7.53)	ND	65.5±0.2	75.8±0.3	ND	ND

Melting temperature T_m determined using the CPM assay²⁸ (mean \pm s.d. for n=3 independent experiments) for the crystallized construct (MT₂-CC), and indicated mutants (in the MT₂-CC background), purified in the absence (apo) or presence (100 μ M) of ligand (mlt, melatonin and 2-PMT, 2-phenylmelatonin). ND, not determined. W129F refers to MT₂-CC but without the F129^{3,41}W mutation. Melting curves are shown in Supplementary Fig. 7.



	Cherezov, Vadim; Katritch, Vsevolod; Roth,
Corresponding author(s):	Bryan

Last updated by author(s): Mar 7, 2019

Reporting Summary

Nature Research wishes to improve the reproducibility of the work that we publish. This form provides structure for consistency and transparency in reporting. For further information on Nature Research policies, see Authors & Referees and the Editorial Policy Checklist.

$\overline{}$					
Ç	tっ	11	ist	т.	\sim
٠,	10		ורו	- 1	

For	or all statistical analyses, confirm that the following items are present in the figure legend, table legend, main text, or Methods section.							
n/a	Confirmed							
	$oxed{oxed}$ The exact sample size (n) for each experimental group/condition, given as a discrete number and unit of measurement							
	🔀 A statement on whether measurements were taken from distinct samples or whether the same sample was measured repeatedly							
\boxtimes	The statistical test(s) used AND whether they are one- or two-sided Only common tests should be described solely by name; describe more complex techniques in the Methods section.							
\boxtimes	A description of all covariates tested							
\boxtimes	A description of any assumptions or corrections, such as tests of normality and adjustment for multiple comparisons							
	A full description of the statistical parameters including central tendency (e.g. means) or other basic estimates (e.g. regression coefficient) AND variation (e.g. standard deviation) or associated estimates of uncertainty (e.g. confidence intervals)							
\boxtimes	For null hypothesis testing, the test statistic (e.g. <i>F</i> , <i>t</i> , <i>r</i>) with confidence intervals, effect sizes, degrees of freedom and <i>P</i> value noted Give <i>P</i> values as exact values whenever suitable.							
\boxtimes	For Bayesian analysis, information on the choice of priors and Markov chain Monte Carlo settings							
\boxtimes	For hierarchical and complex designs, identification of the appropriate level for tests and full reporting of outcomes							
\boxtimes	\boxtimes Estimates of effect sizes (e.g. Cohen's d , Pearson's r), indicating how they were calculated							
	Our web collection on <u>statistics for biologists</u> contains articles on many of the points above.							
Software and code								
Poli	cy information abo	ut <u>availability of computer code</u>						
Da	ata collection	XFEL data were collected at the CXI instrument at LCLS using in-house DAQ software.						
Da	ata analysis	Prodrg server (http://davapc1.bioch.dundee.ac.uk/cgi-bin/prodrg/submit.html; queried in 2017-2018) CHARMM-GUI web-server (http://www.charmm-gui.org/; queried in January 2018)						

For manuscripts utilizing custom algorithms or software that are central to the research but not yet described in published literature, software must be made available to editors/reviewers. We strongly encourage code deposition in a community repository (e.g. GitHub). See the Nature Research guidelines for submitting code & software for further information.

v.3.8-6; Pymol v.1.5; MOSFLM v.7.2.1; DirAx v. 1.17; XDS BUILT 20170601; Sculptor v. 2.1; Phenix v. 1.14; Refmac5 v. 5.5

Cheetah v.2017.3; CrystFEL v.0.6.2; Prism v.7.0; CCP4 v.7.0; Phaser v.2.1; COOT v.0.8.8; BUSTER v.2.10.2; CAVER analyst v.2.0; ICM-PRO

GPCRdb (http://gpcrdb.org/; queried in 2015-2018)

MolProbity server (v4.4; http://molprobity.biochem.duke.edu/; queried in 2018) QC Check server (v3.1; https://smb.slac.stanford.edu/jcsg/QC/; queried in 2018) OPM database (http://opm.phar.umich.edu; queried in January 2018) ChEMBL24 database (https://www.ebi.ac.uk/chembl/; queried in 2018)

HHpred server (https://toolkit.tuebingen.mpg.de/#/tools/hhpred; queried in 2017)

UniProt data resource (https://www.uniprot.org/; queried in July 2018)

Data

Policy information about availability of data

All manuscripts must include a <u>data availability statement</u>. This statement should provide the following information, where applicable:

- Accession codes, unique identifiers, or web links for publicly available datasets
- A list of figures that have associated raw data
- A description of any restrictions on data availability

Structure factors and coordinates were deposited in the Protein Data Bank under the following accession codes: 6ME6 (MT2-CC-2-pmt), 6ME7(MT2-CC-H208A-2pmt), 6ME8 (MT2-CC-N86D-2-pmt), 6ME9 (MT2-CC--ramelteon).

$L_{1} \cap$		Lchacitic	roporting
1 1	ш	1-500001110	
	. ~		reporting

Please select the one be	low that is the best fit for your research.	. It you are not sure, read the appropriate sections before making your selection.
∑ Life sciences	Behavioural & social sciences	Ecological, evolutionary & environmental sciences
For a reference conviof the doc	ument with all sections see nature com/document	rs/pr-reporting-summary-flat ndf

Life sciences study design

All studies must disclose on these points even when the disclosure is negative.

No statistical methods were used to predetermine sample size. Thermostability and pharmacological characterization were conducted at least Sample size in n=3 independent experiments and are comparable to other published studies. Wild-type constructs were used as internal controls, resulting in larger number of independent repeats. Diffraction data from thousands of protein crystals were integrated and scaled to ensure 100% completeness of the dataset.

Data exclusions No data were excluded.

All measurements were done in triplicate and all attempts at replication were successful and presented. Replication

This study did not allocate experimental groups thus no randomization was required for the reported experiments. Randomization

Blinding The researchers were not blinded to allocation during experiments and outcome assessment. Blinding was not required for the reported experiments because all functional and structural data were analyzed using the same methods, and results are not subjective.

Reporting for specific materials, systems and methods

We require information from authors about some types of materials, experimental systems and methods used in many studies. Here, indicate whether each material, system or method listed is relevant to your study. If you are not sure if a list item applies to your research, read the appropriate section before selecting a response.

Materials & experimental systems		Me	Methods	
n/a	Involved in the study	n/a	Involved in the study	
\boxtimes	Antibodies	\boxtimes	ChIP-seq	
	Eukaryotic cell lines	\boxtimes	Flow cytometry	
\boxtimes	Palaeontology	\boxtimes	MRI-based neuroimaging	
\boxtimes	Animals and other organisms			
\boxtimes	Human research participants			
\boxtimes	Clinical data			

Eukaryotic cell lines

Policy information about cell lines

Cell line source(s) Cell lines were purchased from the American Type Culture Collection (ATCC). Sf9: ATCC-CRL-1711. HEK293T cells: ATCC CRL-11268.

Authentication The cell lines were authenticated by the supplier (ATCC) using morphology and growth characteristics (for Sf9 and HEK293T), and STR profiling (for HEK293T).

Both Sf9 and HEK293T cells have been tested and shown to be free from mycoplasma (Hoechst DNA strain and Direct Mycoplasma contamination Culture methods employed).

Commonly misidentified lines (See <u>ICLAC</u> register)

No commonly misidentified cell lines were used.

nature research | reporting summary